Spin-Polarized Photoemission

Jürg Osterwalder

Physik-Institut, Universität Zürich, Winterthurerstr. 190, CH-8057 Zürich,
Switzerland
`osterwal@physik.unizh.ch`

Abstract. The principles of angle-resolved photoemission spectroscopy (ARPES)
with spin resolution are outlined, with the emphasis on conceptual clarity and
not on completeness. In Sect. 2, the theoretical ingredients of the photoemission
process are discussed, including the single-particle matrix element as well as the
many-body reaction of the solid as reflected in the spectral function. Experimental
parameters for probing defined electron states within a three-dimensional Brillouin
zone are defined. Sections 3 and 4 list several situations and mechanisms where spin
polarization is produced or reduced in photoemission signals, and describe how they
can be measured. Spin-polarized ARPES data from a ferromagnetic Ni(111) surface
and from the spin-orbit split surface state on Au(111) follow as case studies. Finally,
the future prospects of the technique are assessed.

1 Introduction

The spin of the electron is at the heart of magnetic and other electron cor-
relation phenomena in condensed matter physics. There is a multitude of
experimental techniques that probe the collective behaviour of spins in solids
and the interaction of spins with other degrees of freedom. They all project
out some observable of electronic states but measure an ensemble average
for others. Magnetic resonance techniques operate directly in spin space and
provide detailed information about magnetic moments and spin dynamics.
Magnetic x-ray or neutron scattering are highly sensitive to magnetic order-
ing phenomena and spin structures in real space (see chapters by C. Dufour
and M. Altarelli in this book). Spin-polarized angle-resolved photoemission
(ARPES) is complementary to these techniques and offers unique informa-
tion especially for itinerant magnetic systems. It measures not only the spin
state but also the energy and momentum of such states and is therefore sen-
sitive to spin structures in reciprocal space, in cases where the direction and
magnitude of the electron spin depends on the wave vector. In this sense, it
is a complete experiment that can provide very detailed information e.g. on
the exchange-split bands of itinerant ferromagnets [1].

Ordered spin structures both in real space and in reciprocal space are be-
coming increasingly more important in the context of *spintronics* [2], where
functionalities are introduced in electronic devices that are based on the elec-
tron spin. Vigorous research is now going on worldwide for designing ways

and materials to inject spin-polarized electron (or hole) currents into semi-conductors and for finding ways to manipulate them. A device that illustrates the combination of these concepts is the spin field-effect transistor proposed by Datta and Das [3], where ferromagnetic source and drain electrodes represent simple real space spin structures whereas the momentum dependence of the spin in the active channel is necessary for the control of the spin precession by the electric field of the gate electrode. ARPES with spin resolution is likely to play an important role in the materials-related investigation of these spin-dependent phenomena.

Unfortunately, in order to characterize the spin-polarized band structure of a solid, we cannot simply use the spin of the electrons as a tag and measure independently the photoelectron spectra for spin-up and spin-down electrons, e.g. in the equivalent of a Stern-Gerlach experiment. Unlike neutral atoms, electrons are strongly deflected in magnetic fields. By means of sophisticated arguments it can be shown that these Lorentz forces and the uncertainty principle conspire to render impossible the complete spin separation by magnetic fields [4, 5]. In practice, one therefore exploits the spin-dependence in a scattering experiment in order to characterize the *spin polarization* in a beam of electrons that has been preselected according to energy E and wave vector $\boldsymbol{k}$ by an angle-resolving spectrometer. It is defined as

$$P_I(E, \boldsymbol{k}) = \frac{I_\uparrow(E, \boldsymbol{k}) - I_\downarrow(E, \boldsymbol{k})}{I_\uparrow(E, \boldsymbol{k}) + I_\downarrow(E, \boldsymbol{k})} \, , \qquad (1)$$

where $I_{\uparrow,\downarrow}(E, \boldsymbol{k})$ represent the cleanly spin-resolved ARPES spectra for a spin quantization axis defined by the scattering geometry [5]. We refer to Section 4 for more details on how the spin polarization is extracted from left-right scattering asymmetries. At this point we emphasize that the measured quantities are the spin-integrated spectrum $I_M(E, \boldsymbol{k}) = I_\uparrow(E, \boldsymbol{k}) + I_\downarrow(E, \boldsymbol{k})$ and the spin-polarization $P_I(E, \boldsymbol{k})$, from which the spin-dependent spectra can be recovered as

$$I_{\uparrow,\downarrow}(E, \boldsymbol{k}) = I_M(E, \boldsymbol{k})(1 \pm P_I(E, \boldsymbol{k}))/2 \, . \qquad (2)$$

Does the spin-polarized spectrum reflect the true spin polarization of the electronic states in the system under study? Unfortunately, this is not necessarily true. In Sect. 3, several different mechanisms inherent in the photoemission process are discussed that affect the spin polarization that is experimentally observed. One is due to strong correlation effects that often occur in magnetic materials when the photoeffect produces a hole in a localized level. Likewise, spin-dependent electron-electron scattering effects of the photoelectron when leaving the sample surface can reduce one spin channel $I_{\uparrow,\downarrow}(E, \boldsymbol{k})$ with respect to the other. Moreover, the interaction of the photoelectrons with other elementary excitations in the solid (phonons, magnons) can be different in both spin channels. Finally, chiral measurement geometries can introduce dichroic photoemission matrix elements that affect the

two spin channels differently. All these effects can hamper the characterization of spin-resolved bands in the ground state. They are in most cases not well known. On the other hand, they provide interesting opportunities for studying spin-dependent many-body interactions in solids.

2 Angle-Resolved Photoemission Spectroscopy (ARPES) and Fermi Surface Mapping

In order to understand how photoemission spectra relate to the electronic band structure and elementary excitation spectra, and how spin polarization gets transferred from the initial state into the photoelectron final state, we need to establish the theoretical foundations of the method. In a general sense the photoemission process promotes the solid, containing N electrons within the interaction region, from the quantum mechanical N-electron state $\Psi_i(N)$ to the photoexcited $(N-1)$-electron state $\Psi_f(N-1, \boldsymbol{k_i})$ with a hole (or missing electron) in quantum state $\boldsymbol{k_i}$. At the same time, a photoelectron is produced in a free-electron state $\phi_f(\epsilon_f, \boldsymbol{k})$ propagating in vacuum (see below for the relation between the two wave vectors $\boldsymbol{k}$ and $\boldsymbol{k_i}$). From Fermi's Golden Rule the process occurs with a probability

$$ w \sim |\langle \Psi_f(N-1, \boldsymbol{k_i})\phi_f(E, \boldsymbol{k})|\boldsymbol{A} \cdot \boldsymbol{p}|\Psi_i(N)\rangle|^2 \delta(E_f - E_i - h\nu) , \qquad (3) $$

where the operator $\boldsymbol{A} \cdot \boldsymbol{p}$ describes the interaction between the vector potential $\boldsymbol{A}$ of the absorbed photon and the electron momentum $\boldsymbol{p}$, and E_i and E_f are the total energies of the system before and after the emission process (including the photoelectron energy ϵ_f) [1]. The matrix element can be factorized into a one-electron matrix element $M_{i,f} = \langle \phi_f(\epsilon_f, \boldsymbol{k_f})|\boldsymbol{r}|\phi_i(\epsilon_i, \boldsymbol{k_i})\rangle,$[1] connecting the photoelectron with the initial one-electron state $\phi_i(\epsilon_i, \boldsymbol{k_i})$, times an overlap integral $\langle \Psi_f(N-1, \boldsymbol{k_i})|\Psi_i(N-1, \boldsymbol{k_i})\rangle$ of $(N-1)$-electron states involved before and after the removal of an electron in quantum state $\boldsymbol{k_i}$. In the process, the $(N-1)$-electron state finds itself suddenly in a changed potential with one electron missing, and in the so-called *sudden approximation* $\Psi_f(N-1, \boldsymbol{k_i})$ is expanded in Eigenstates $\tilde{\Psi}_f(N-1, \boldsymbol{k_i})$ of the perturbed Hamiltonian: $\Psi_f(N-1, \boldsymbol{k_i}) = \sum_s c_s \tilde{\Psi}_{f,s}(N-1, \boldsymbol{k_i})$. Here, the values $|c_s|^2$ describe the probability for finding the $(N-1)$-electron system in the excited state $\tilde{\Psi}_{f,s}(N-1, \boldsymbol{k_i})$ with label s after the removal of electron $\boldsymbol{k_i}$. In a solid, there is a continuum of excited states, including electronic, phononic and also magnetic excitations, and these probabilities are thus described by a continuous spectral function $A(\boldsymbol{k_i}, E)$, where E is the excitation energy of he system (i.e. $E = 0$ corresponds to the ground state of the $(N-1)$-electron system

---

[1] Due to commutation relations, and if the vector potential $\boldsymbol{A}$ varies slowly over atomic dimensions, the operator $\boldsymbol{A} \cdot \boldsymbol{p}$ in these matrix elements can be replaced by the operator $\boldsymbol{r}$ [1].

with total energy E_f^0). For each wave vector $\boldsymbol{k_i}$ the spectral function describes the excitation spectrum produced by the sudden presence of a hole in state $\boldsymbol{k_i}$. There are powerful theoretical concepts for the calculation of $A(\boldsymbol{k_i}, E)$ including electron-electron, electron-phonon, and electron-magnon interaction, although the actual computations are not a trivial task. The photoemission intensity measured along a direction (θ, ϕ) can be written as

$$I(\epsilon_f, \boldsymbol{k}) \sim |M_{i,f}|^2 \times A(\boldsymbol{k_i}, E) \times \delta(\boldsymbol{k_i} - \boldsymbol{k_f} + \boldsymbol{G}) \times \delta(\epsilon_f + E_f^0 + E - E_i - h\nu) \ . \quad (4)$$

The two δ-functions represent energy and momentum conservation. In a one-electron picture where excitations of the many-body system are neglected ($E = 0$), the total-energy difference $E_f^0 - E_i$ equals the binding energy ϵ_B of the initial-state one-electron wave function and the δ-function simply ensures that $\epsilon_f = h\nu - \epsilon_B$ which is often referred to as the Einstein relation.

The second δ-function connects the wave vectors $\boldsymbol{k_i}$ and $\boldsymbol{k_f}$: In the case of itinerant states in crystalline solids, crystal momentum $\hbar \boldsymbol{k_i}$ is a good quantum number. It is conserved in the photoemission process up to a reciprocal lattice vector $\boldsymbol{G}$, because the photon momentum can usually be neglected in a typical ARPES experiment.[2] A complication arises due to the fact that the photoelectron is measured in vacuum, i.e. after it has left the potential range of the sample. The detection angles θ_m and ϕ_m, together with a kinetic energy value ϵ_f define a wave vector $\boldsymbol{k}$ of a free electron in vacuum:

$$\boldsymbol{k} = \frac{1}{\hbar} \sqrt{2m\epsilon_f} \times (\sin\theta_m \cos\phi_m, \sin\theta_m \sin\phi_m, \cos\theta) \ , \quad (7)$$

where m is the electron mass. The question of how $\boldsymbol{k}$ relates to the wave vector $\boldsymbol{k_f}$ of the photoelectron inside the crystal represents a fundamental difficulty in ARPES, where the photoelectron has to penetrate the surface barrier of the solid. The crystal periodicity parallel to the surface ensures that the wave vector components parallel to the surface plane are conserved: $\boldsymbol{k}_\parallel = \boldsymbol{k_{f,\parallel}} + \boldsymbol{g}$.[3] In the direction perpendicular to the surface, the periodicity of the crystal lattice is truncated abruptly by the surface potential step, where the average potential rises from the inner potential $-V_0$ in the solid to zero in vacuum. In the so-called *free-electron final-state approximation*, where the

---

[2] Convenient conversion formulas from energies E_{kin} or $h\nu$ (in eV) to wave numbers $|\boldsymbol{k}|$ in $\mathring{A}^{-1}$ for free electrons and photons, respectively, are:

$$|\boldsymbol{k}| = 0.5123 \times \sqrt{E_{kin}} \approx 0.51 \times \sqrt{E_{kin}} \quad (5)$$

and

$$|\boldsymbol{k}| = 0.5068 \times h\nu \times 10^{-3} \approx 0.51 \times h\nu \times 10^{-3} \ . \quad (6)$$

[3] A surface reciprocal lattice vector $\boldsymbol{g}$ can appear in cases where the surface is reconstructed, showing a periodicity that is different from the truncated bulk crystal, and leading to so-called surface Umklapp scattering.

photoelectron state in the solid is treated like a single plane wave with wave vector

$$\boldsymbol{k_f} = \frac{1}{\hbar}\sqrt{2m(\epsilon_f + V_0)} \times (\sin\theta\cos\phi_m, \sin\theta\sin\phi_m, \cos\theta) , \qquad (8)$$

the consequence is a reduction of the component $\boldsymbol{k}_\perp$ perpendicular to the surface. This leads to a refraction of the photoelectron wave that can be described by Snell's law:

$$\sin\theta = \sin\theta_m \sqrt{\frac{\epsilon_f}{\epsilon_f + V_0}} . \qquad (9)$$

Here, the electron energy is referenced to the vacuum level. Typical values for V_0 are of the order of $10\,\mathrm{eV}$, and for low energies refraction angles can be substantial.

This may seem like a crude approximation for a photoelectron propagating through a periodic potential, but it has nevertheless proven to be quite successful.[4]

A fundamental difficulty arises because photoelectrons have a relatively short inelastic mean free path. This means that only those electrons originating from a thin selvage region typically a few atomic layers thick contribute to the true spectrum, while electrons originating from deeper within the crystal constitute a smoothly rising inelastic background at lower kinetic energies. But it also means that $\boldsymbol{k}_\perp$ is no longer well defined but smeared out. This severely limits the precision at which $\boldsymbol{k_f}$ can be measured and has to be carefully considered when interpreting ARPES data. The problem does not occur in two-dimensional electronic states where $\boldsymbol{k}_\parallel$ is the only relevant quantum number.

The two δ-functions in (4), providing a kinematical description of photoemission processes, represent a very stringent condition under which photoemission intensity can be observed, especially when excitations in the many-body system are neglected and $\epsilon_B = E_f^0 - E_i$, where $\epsilon_B(\boldsymbol{k_i})$ represents the single-particle band structure of the solid[5]. The conventional picture of direct

---

[4] In the traditional *three-step model* of photoemission, the process is described as a sequence of three steps: (1) photoexcitation of an electron into an unoccupied state within the sample band structure, (2) propagation of this band state to the surface, undergoing also inelastic losses, and (3) penetration of the surface potential step and coupling to a free-electron state in vacuum. In the more accurate *one-step model* the entire process is coherently described in one single step, with a final state wave function that considers all scattering events of the photoelectron within the surface region, including inelastic processes, and the coupling to the vacuum state in a so-called *time-reversed low-energy electron diffraction (LEED) state*. It appears that the use of a free-electron final state in the three-step model corrects for some inadequacies of the former approach [6].

[5] In principle, many-body effects are included implicitly because the energy E_f^0 is the lowest energy of the $(N-1)$-electron system in the excited state $\tilde{\Psi}_{f,s}(N-$
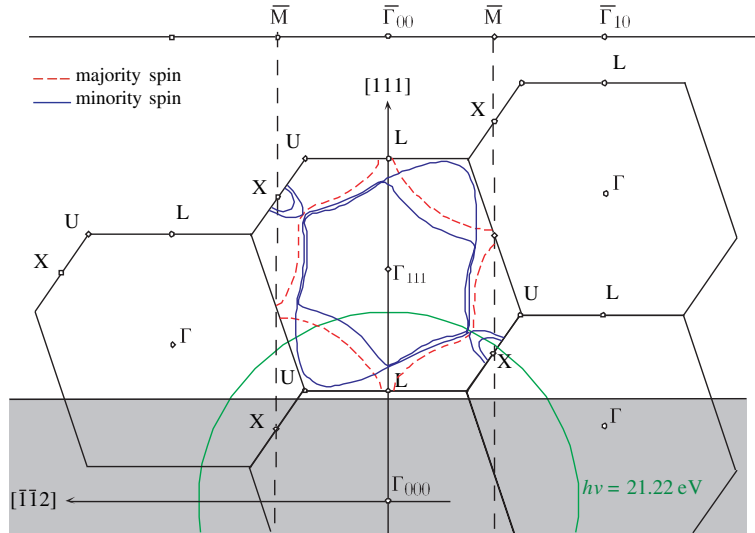
Fig. 1. Schematic diagram for k-space mapping experiments.In the free-electron final-state approximation direct transitions are expected where the final state sphere (large circle centered at Γ_{000}) intersects with an initial state band in the extended zone scheme. $\boldsymbol{k}_{\parallel}$ of these intersection points is conserved throughout the photoemission process. The grey area in $\boldsymbol{k}$-space is not accessible due to total internal reflection according to (9) (From [7])

transitions results [1]: in a band structure plotted in the *reduced zone scheme* the conservation of wave vectors up to a reciprocal lattice vector means that an electron is transferred vertically, i.e. at constant crystal momentum, from an initial state band to a final state band $\epsilon_B^i(\boldsymbol{k_i}) \rightarrow \epsilon_B^f(\boldsymbol{k_i})$ with energy levels separated by

$$\epsilon_B^f(\boldsymbol{k_i}) - \epsilon_B^i(\boldsymbol{k_i}) = h\nu \ , \tag{10}$$

i.e. by the photon energy. In the free-electron final-state approximation, the upper level is connected to the value of $\boldsymbol{k_i}$ by the simple relation

$$\epsilon_B^f(\boldsymbol{k_i}) = \epsilon_B^f(\boldsymbol{k_f} - \boldsymbol{G}) = \hbar^2|\boldsymbol{k_f}|^2/2m \ . \tag{11}$$

The geometrical implications of these equations is illustrated in Fig. 1, where a planar section through the reciprocal space of a Ni crystal is plotted. The geometry and the periodicity are defined by the Brillouin zones given in the *repeated zone scheme*. In one of the zones, centered at the reciprocal lattice point $\boldsymbol{G} = \Gamma_{111}$, the sections through the Fermi surfaces defined by the Ni

---

1, $\boldsymbol{k_i}$) with electronic charges rearranged in order to screen the photohole $\boldsymbol{k_i}$. In highly itinerant cases, this effect may be small [1], and $\epsilon_B(\boldsymbol{k_i})$ is quite close to a single-particle band structure. For more localized hole states the deviations may become substantial (see Sect. 3.2).

band structure are given. These curves are defined by the condition $\epsilon_B^i(\boldsymbol{k_i}) = \epsilon_F$ where ϵ_F is the Fermi energy. The large circle centered at $\boldsymbol{G} = \Gamma_{000}$, which we may term the *measurement sphere*, represents the free-electron final states for the photon energy $h\nu = 21.22\,\text{eV}$ with a radius calculated according to Equations (10) and (11). Measurement sphere and Fermi surface sections thus represent states in $\boldsymbol{k}$-space with the correct energy separation, and whereever they intersect, momentum is conserved. As is obvious from this figure, there are only few points in this plane that qualify for the kinematics according to (4). If other vertical planes, obtained by azimuthal rotations about the surface normal (here the [111] direction), are considered in an equivalent way, it becomes clear that these few points will form continuous lines on the measurement sphere.

This simple kinematical concept is borne out nicely by the data shown in Fig. 2a, which shows a complete *Fermi surface map* measured on a Ni(111) surface at a photon energy of $h\nu = 21.22\,\text{eV}$. In this figure, photoemission intensities at the Fermi energy are plotted as gray scale values for a complete hemispherical set of emission angles ($\theta_m = [0..88°], \phi_m = [0..360°]$), projected parallel onto the $\boldsymbol{k}_\parallel$-plane. It exhibits a number of well-defined contours which are well reproduced in a theoretical plot (Fig. 2b) that was obtained by plotting all intersections of measurement sphere and Fermi surface in the same projection. The latter was obtained within the standard band structure package Wien2k [8]. The excellent agreement in most details demonstrates
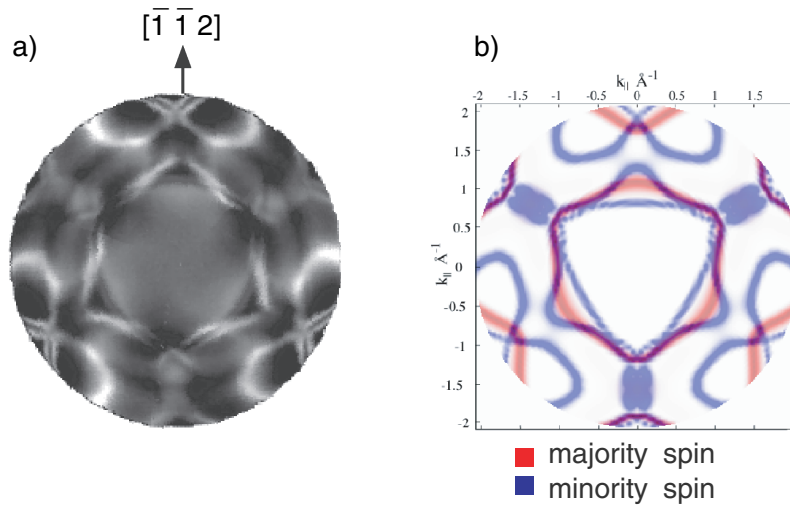

Fig. 2. (a) He Iα excited Fermi surface map ($h\nu = 21.21\,\text{eV}$) from Ni(111). A $\boldsymbol{k}_\parallel$ projection of the raw data is presented in a linear grey scale, with highest intensities in white, lowest in black. In (**b**) the corresponding spin-polarized band structure calculation is displayed, showing Fermi level crossings at the same $\boldsymbol{k}_\parallel$ locations as in the measurement (a). Majority spin bands are shown in red, minority spin bands in grey (From [10], with improved experimental data by W. Auwärter)

that this simple kinematical interpretation of ARPES data, including the use of the free-electron final-state model, is a viable concept in order to measure and identify band structures. Refined models using more realistic final states are under investigation, but they have yet to prove their general applicability [9].

The experimental Fermi surface contours of Fig. 2a appear with different brightness values (photoemission intensities) and with different widths. These properties are not explained within the kinematical picture. They have to do with state- and k-dependent matrix elements $M_{i,f}$ (intensities) and with broadening of $k_\perp$ as well as issues related to the spectral function $A(k_i, E)$ (widths) [6].

The basic ingredients in the formation of valence photoemission signals have now been considered. In the next section it will be discussed how a measured spin polarization in such signals relates to that in the initial state, and which processes produce or reduce spin polarization.

3 Sources of Spin Polarization in ARPES Data

The photon of the exciting light does not directly couple to the electron spin, and one might expect that the spin polarization measured in a spin-resolved photoemission experiment should directly reflect the spin polarization of the initial states under study. However, indirect coupling occurs in the process due to several mechanisms involving a spin-dependent reaction of the remaining $(N-1)$-electron system (if it is strongly spin polarized), spin-orbit effects and spin-dependent elastic exchange scattering (spin-polarized photoelectron diffraction) in the photoelectron final state, or finally spin-dependent inelastic scattering processes during electron transport to the surface.

3.1 Spin-Polarized Initial States

The band-structure calculation that formed the basis for plotting the Fermi surface contours in Fig. 2b was fully spin-polarized. In a ferromagnetic material, spin-up and spin-down electrons receive their label ($\uparrow, \downarrow$) from the respective band filling (minority or majority electrons), and the exchange splitting develops as a consequence of the exchange and correlation potentials. The resulting contours can thus be labeled in a color code according to their spin. At places where the contours do not overlap one would thus expect a spin polarization of 100%. Spectral overlap and poorly defined magnetization state of a sample can reduce this value considerably (see Sect. 5.1). A demagnetized sample produces zero spin polarization, because spin-polarization values from

---

[6] In the theoretical contours of Fig. 2b, the width is a consequence of the finite momentum shell around the ideal measuring sphere that had to be defined in order to produce continuous contours at the given sampling density.

different magnetic domains average out in the fixed spin detection geometry. Conversely, such experiments can be used for magnetometry [11].

Spin-splittings of bands can not only arise due to electron exchange interactions, but also from the spin-orbit interaction (see Sect. 5.2), which couples the spin to the symmetry of the lattice. This forms the basis for the magnetic anisotropy in exchange-coupled systems, and it can lead to non-trivial spin structures in spin-orbit coupled systems, where the *direction* and the *magnitude* of the spin-polarization vector is k_i-dependent. In this case, the observation of spin polarization from spin-split bands is not dependent on a net magnetization of the sample. On the other hand, it is necessary to introduce spin polarization as a vectorial quantity, defined as the vector of expectation values of the spin operators for a given state or ensemble of states

$$\boldsymbol{P} = \frac{2}{\hbar}(\langle S_x \rangle, \langle S_x \rangle, \langle S_x \rangle) \,, \tag{12}$$

where the normalization constant $2/\hbar$ makes sure that the absolute value is $P \leq 1$ [5].

3.2 Effects of Electron Correlation on Spin Polarization

In materials with electronic states that are rather localized and where the Coulomb interactions between the electrons are thus strong, the extraction of one electron can lead to severe many-body excitations of the system. This means that the spectral function appearing in (4) leads to a strong redistribution of photoelectron intensities over the energy axis, and the photoemission spectrum measured at a particular wave vector k_f no longer reflects a single-particle state with sharp energy $\epsilon_B^i(k_i)$. The typical effects are threefold [1,12]: the single-particle peak shifts to lower binding energy and receives a finite width, and at higher binding energy a much broader distribution of spectral weight occurs. The first two effects suggest that the missing electron (hole) can be described as a coherent *quasiparticle* (with defined energy and with momentum k_i) forming the lowest-energy state of the $(N-1)$-electron system (hence the *relaxation shift*), which has a short life time due to the strong interactions (hence the finite width). The broader distribution reflects the occurrence of a continuum of excited many-body states lacking the defined energy-momentum relation of a particle. It is thus termed the *incoherent* part of the spectral function.

In a ferromagnetic material these effects can be strongly spin dependent. This is illustrated in Fig. 3, taken from a recent comparative investigation of photoemission spectra and spectral functions in cobalt metal [13]. Panels (a) and (c) show the results of a spin-resolved band structure, calculated along a line in k_i-space that corresponds to a photoemission data set presented in the same study (not shown). The typical picture of an itinerant ferromagnet is displayed, with two rather similar band structures for the two spin channels
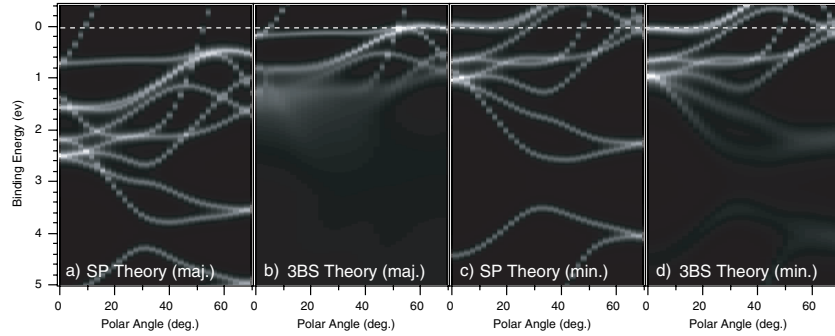
Fig. 3. Comparison of spin-resolved single-particle band structure and many-body quasiparticle spectral function for the same wave vector region in hexagonal close-packed Co. Binding energies are referenced to the Fermi level, and wave vectors are described in terms of polar angles θ_m in a photoemission experiment on a (0001) oriented thick Co film. Panels (**a**) and (**b**) compare single- and quasiparticle spectra for majority ($\downarrow$) electrons, panels (**c**) and (**d**) those for minority ($\uparrow$) electrons (from [13])

and with a large exchange splitting of the order of $1.5\,\mathrm{eV}$ between the two. Clearly, one expects large spin polarization values in photoemission from such spin-split bands where they do not overlap. However, the many-body calculation (panels (b) and (d)) conveys a completely different picture. It uses a simple model on top of the detailed band structure calculation where the missing electron interacts strongly with one additional electron-hole pair in the so-called *three-body scattering approximation*. The result shows that there is a severe renormalization of band positions and line widths in the majority channel, while the effects in the minority channel are only minor. In a *strong ferromagnet* like Co, where the majority d band is completely filled, this asymmetry arises for the following reason: electron-hole pairs can only be created in the minority channel (see Fig. 4). A hole produced due to photoemission in the majority channel is accompanied by the full phase space of electron-hole pair excitations in the minority d band, thus rendering the quasiparticle renormalization very strong. For a photohole in the minority d band, the configurations for electron-hole pairs are restricted, because there are now two holes that interact strongly and repulsively. The overall result of this asymmetry is that both spin channels produce spectral functions that are rather similar, which leads to the expectation of strongly reduced spin polarization in photoemission data from cobalt. On the experimental side, spin-integrated spectra measured along the same line in $\boldsymbol{k_i}$-space [13] are in good agreement with these quasiparticle spectra, and so are spin-resolved photoemission spectra for thick Co(0001) films measured at normal emission ($\theta_m = 0°$) with the same photon energy [14, 15].
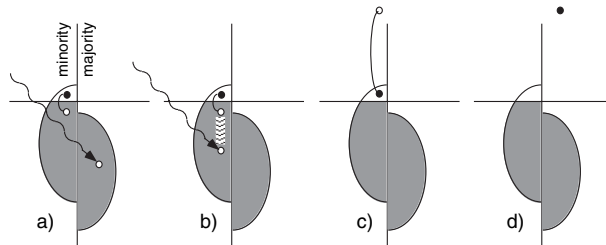
Fig. 4. Schematic representation of the interactions involved in several spin-dependent processes within the d band of a strong ferromagnet. (**a**) photoemission in the majority spin band, (**b**) photoemission in the minority spin band, (**c**) inelastic scattering into the minority channel, and (**d**) inelastic scattering into the majority channel. In (a) and (b), electron-hole pair excitation is possible only in the minority channel. In (d) there is no spin-conserving inelastic scattering into empty d states. Situations (c) and (d) refer to Sect. 3.4

3.3 Spin-Polarization Introduced by the Photoexcitation Process

Several distinct mechanisms have been identified that can introduce or change spin polarization in photoemission intensities through spin-selectivity in the matrix element $M_{i,f}$ of (4). They are most conveniently studied in photoemission from non-magnetic samples where no spin-polarization is present in the initial states. The most robust effects are produced when *circularly polarized light* is used, where spin-polarized emission is quite commonly observed. Optical pumping of spin-orbit split initial state bands leads to asymmetric occupation of final-state spin states [16]. A spin-polarized electron source based on a GaAs photocathode and illuminated by circularly polarized laser light produces electron beams with 43% spin polarization [17]. Also at higher photon energies substantial spin polarization can be observed, especially in the heavier elements [18].

Also excitation by *linearly polarized light* can introduce spin-dependent matrix-element effects and thus produce spin polarization in photoemission from non-magnetic samples. The mechanisms here include spin-dependent transmission through the surface of solids with non-vanishing spin-orbit coupling [19] and more subtle effects that showed up first in photoemission calculations within the *one-step model* [20–22] and were later observed experimentally [23–25]. The mechanisms behind the latter effects are related to spin-orbit induced hybridization of initial-state wave functions, and their occurrence depends strongly on the symmetry of the solid and of the particular surface, as well as the absolute directions of photon incidence and polarization and electron emission. In materials containing ions with finite magnetic moments, intra-atomic multiplet splittings due to final-state $L-S$ term splittings are an important internal source of spin polarization [26], mostly discussed in the context of core levels. Such moments can also give rise to spin-polarized photoelectron diffraction effects [27], both in core and valence

photoemission: the scattering potential of the photoelectron within the ionic environment depends on the relative orientation of the electron spin and the magnetic moments.

It is hard to get an intuitive picture of the relative importance of all these mechanisms, but one has to be aware that such effects are there in principle. How much they may blur the characterization of spin polarization and spin structure in the initial state is not clear at the moment.

3.4 Spin-Polarization Induced or Reduced During Electron Transport

The theoretical expression for photoemission intensities given in (4) reflects the so-called *intrinsic* contribution to the measured intensity, including the photoemission process and, in principle, the full multiple-elastic-scattering photoelectron final state. It considers the *extrinsic* inelastic scattering processes that remove photoelectrons from the elastic channel only implicitly by assuming final state wave functions that decay exponentially away from the surface into the crystal. Extrinsic inelastic processes occur along the way as photoelectrons propagate towards the surface, and collected energy losses move them from the *elastic peak position* to a smoothly rising inelastic background on the higher binding energy side, underneath the intrinsic spectrum. The photoelectron inelastic mean free path $\lambda_i(\epsilon_f)$ defines the surface sensitivity of photoemission as a probe for the electronic structure of solids, because the electrons appearing in the inelastic background no longer reveal the spectral information contained in the intrinsic spectrum due to the random nature of the inelastic processes. Inelastic scattering cross sections are very high, and values of $\lambda_i(\epsilon_f)$ are thus of the order of a few Å. As it turns out, inelastic processes can be an important source for photoelectron spin polarization or depolarization as well.

In a ferromagnet, this latter effect can be described simply by considering two different values $\lambda_i^{\uparrow}(\epsilon_f)$ and $\lambda_i^{\downarrow}(\epsilon_f)$ for photoelectron spins antiparallel or parallel to the sample magnetization, respectively. Evidence for the inequivalence of $\lambda_i^{\uparrow}(\epsilon_f)$ and $\lambda_i^{\downarrow}(\epsilon_f)$ has come from experiments involving thin ferromagnetic overlayers on top of non-magnetic substrates [15, 28]. In spin-resolved detection, a distinctive valence photoemission signal is attenuated more rapidly in the minority spin channel. In the case of Co(0001) films grown on W(110), values of $\lambda_i^{\downarrow} = 6.6\,\text{Å}$ and $\lambda_i^{\uparrow} = 9.0\,\text{Å}$ were extracted from the thickness dependent signal attenuation for $\epsilon_f = 14\,\text{eV}$ (referenced to the Fermi energy). This asymmetry is brought about by the different density of empty d-states that are available for scattering in the two spin channels (see Fig. 4c and d). An empirical law by Siegmann relates the spin-asymmetry in the total inelastic scattering cross section to the paramagnetic occupation number n of the d shell and its change Δn in each spin channel in forming the ferromagnetic state [29]. This simple model works quite successfully for the entire series of $3d$ transition metals.

This spin-dependent transport effect was also demonstrated in transmission experiments where electron beams of controlled spin polarization were passed through self-supporting and magnetized Au/Co/Au tri-layers, and has also been termed the *spin- filter effect* [30]. If the spin polarization vector P of the incident electron beam is perpendicular to the magnetization M of the sample, the vector P of the elastically transmitted electron beam points into a different direction when it emerges from the sample. This is due to the elastic and inelastic interactions of the electrons inside the ferromagnet. Due to the elastic interaction mediated by the exchange field, P precesses around the axis of M while it rotates into the direction of M due to inelastic yet spin conserving scattering. The total motion of P depends on the electron energy and is characteristically different with Fe, Co, and Ni [31].

The first experiments with spin-polarized electrons were much less sophisticated and designed to examine whether spin polarization appears at all with photoemitted electrons. Quantum theory had made it clear that the magnetization in Fe, Co, and Ni must be predominantly generated by the spin polarization of the metallic electrons, and that the spin polarization should be preserved in the process of emission. While the first attempts to detect the spin polarization of photoelectrons failed [32, 33], it became obvious soon thereafter that with atomically clean surfaces, photoelectrons from all kinds of ferromagnetic materials exhibit sizeable spin polarization [34, 35]. However, almost all theories on magnetism predict that the spin polarization of threshold photoelectrons should be negative (i.e. minority in character) in Co and Ni, because the majority spin states must be located well below the Fermi-level, separated by an energy gap called the Stoner gap. The magnitude of the magnetic moment and the number of available d-electrons dictate that the majority states are completely occupied in both cases. Yet threshold photoelectrons show negative spin polarization only with Ni [36] but not with Co [37, 38]. Today, this is understood by the spin-filter effect active in transport of the photoelectrons to the surface, removing the minority spins by scattering on the minority spin holes in the 3d-states, and enhancing the positive polarization of the photoemitted electrons. The spin-filter effect is much stronger in Co due to the larger density of minority spin holes [29].

A seminal experiment showing how overwhelming this spin-filter effect can be with low-energy threshold electrons uses the spin polarization of Auger electrons as well as the polarization of low energy cascade electrons from a Fe(100) surface covered with one monolayer of Gd [39]. The $N_{45}N_{67}N_{67}$ Auger electrons excited from the $4f^7$-states of Gd are spin polarized antiparallel to the electrons emitted from the $M_{23}M_{45}M_{45}$ Auger electrons of the Fe-substrate, as expected due to the well known antiparallel coupling of the Gd- and Fe-magnetic moments. In contrast, the low-energy cascade electrons emerging at threshold already show the reversed polarization of the Gd overlayer, proving that most of their formation process occurs in one single Gd layer. This much shorter escape depth of low-energy electrons [40] excludes

earlier interpretation of the photoelectron spin polarization in terms of quasi elastic spin flip scattering [41, 42]. Rather, the polarization of threshold photoelectrons must be attributed to the spin conserving scattering on the large and spin-polarized density of $5d$ holes of the rare earth metals.

One has thus to be aware that the spin polarization of photoelectrons may be considerably altered in transport to the surface if unoccupied d-states are present. With monolayer or sub-monolayer coatings of, e.g., the alkali metals, the spin polarization is not affected [41], which has been used in a number of interesting photoemission experiments [43, 44] to reduce the photoelectric work function.

4 Measurement of Spin Polarization in ARPES

In a spin-resolved ARPES experiment, an electrostatic energy analyzer provides an energy and momentum selected photoelectron beam at the exit aperture while preserving the spin polarization and spin orientation. As pointed out earlier, electrons within this prepared beam cannot be separated according to their spin along a predefined axis like neutral atoms in a Stern-Gerlach experiment. Therefore, rather inefficient spin detection schemes that are based on spin-dependent scattering processes need to be applied in order to determine the spin polarization. Among these, Mott scattering and polarized low-energy electron diffraction (PLEED) are the most frequently used. Two detectors placed symmetrically with respect to the beam axis measure the left-right asymmetry of intensities backscattered from a suitable target:

$$A_x = \frac{(I_L - I_R)}{(I_L + I_R)} \ . \tag{13}$$

The scattering asymmetry results from the spin-orbit interaction in the target region and depends on the polarization component perpendicular to the scattering plane (here x). The asymmetry measured for a 100% polarized electron beam depends on the electron energy, the target material and thickness, and the scattering angle; it is called the Sherman function S [5]. Usually it is calibrated experimentally, and it can then be used to determine the spin polarization P_x of an electron beam along a defined axis from the measured scattering asymmetry A_x in the related scattering plane (here the yz plane):

$$P_x = A_x/S \ . \tag{14}$$

Sherman functions can take values of almost up to 0.5 theoretically, and for ultimately thin target foils that avoid multiple elastic or inelastic scattering events. On the other hand, only a small fraction I/I_0 of the electrons in the beam are backscattered into the detectors. For judging the efficiency of a spin detector, the figure of merit $\epsilon = (I/I_0)S^2$ reflects both of these aspects. Figures of merit for typical spin polarimeters are in the range of 10^{-4} to

10^{-3}. It is the relevant quantity for establishing the statistical error in a polarization measurement:

$$\Delta P_x = 1/\sqrt{\epsilon I_0} \ . \tag{15}$$

In deciding upon the particular choice of spin detector, the figure of merit ϵ is not the only all-important factor. Another criterion is temporal stability. The level of complexity of a typical photoemission experiment, including sample preparation, is such that one favours a polarimater that produces reproducible absolute spin polarization values without frequent recalibration or repeated target preparation. Although the PLEED detectors can have high figures of merit, the low electron energies of typically 100 eV make the Sherman function dependent on the condition of the target surface that can deteriorate over the period of one or several photoemission measurements. The target surface needs to be periodically reestablished. This is the main reason why the rather inefficient high-energy Mott detectors, where the scattering occurs at 50–120 keV, are used in most cases. Here, the high-energy electrons penetrate the target foil of several hundred nanometers thickness, which usually consists of Au or some other heavy element providing a strong spin-orbit interaction. These devices can thus be operated over weeks and months under stable conditions.

In ARPES, and specifically in Fermi surface mapping experiments, the need arises for full three-dimensional spin polarimetry. In order to access arbitrary locations in momentum space, the sample needs to be brought into the corresponding orientations relative to the spectrometer. For a magnetized sample, the magnetization vector, and thus the spin quantization axis, is rotated relative to the spin detector. Likewise, for spin-orbit induced spin structures, where the spin vector depends on the electron momentum, the spin polarization vector can have components in all three spatial directions. Moreover, since the total spin polarization vector need not have unity length, one cannot deduce a third component from measuring the other two.

In a single Mott polarimeter, two pairs of detectors can be placed in two orthogonal scattering planes, thus measuring the two spin components transverse to the beam direction. By combining two of these devices in an othogonal geometry, with an electrostatic beam switcher in front of them (see Fig. 5), a fully three-dimensional spin polarimeter has been built [7]. The scattering planes are placed such that the two Mott polarimeters share a common spin quantization axis (z axis). The redundancy along this axis provides useful consistency checks. The beam is switched at typically 1 Hz between the two devices. The three components of the spin polarization vector thus measured in the coordinate frame of the polarimeter can be transformed into a spin polarization vector in the sample coordinate frame by means of a rotation matrix containing the emission angles θ_m and ϕ_m selected in order to reach the specific point $\boldsymbol{k_i}$ in momentum space [7].

For spin-polarized ARPES experiments on exchange-split bands from magnetized samples, the proper control of the magnetization state represents
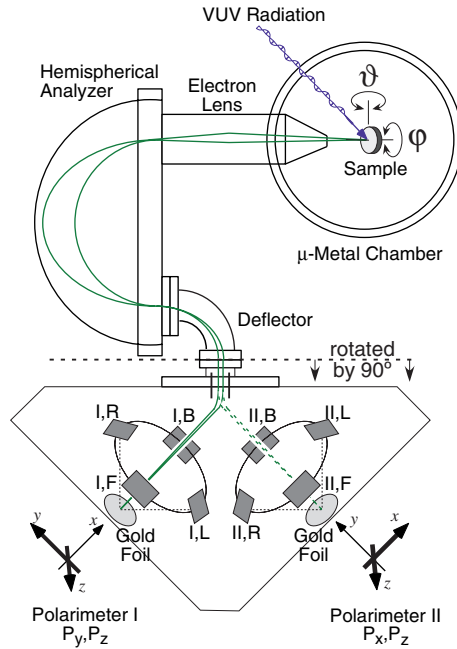
Fig. 5. Schematic view of the three-dimensional polarimeter [7]. Electrons that are photoemitted from a sample by ultraviolet radiation are energy and angle selected by an electrostatic analyzer and detected in two orthogonal Mott polarimeters (named polarimeter I and II). In an electrostatic beam deflection system the spin direction is conserved and polarimeter I measures the polarization components P_y and P_z, while polarimeter II measures P_x and P_z. The beam is switched between the two in order to allow quasi-simultaneous data collection. In the figure, the polarimeter system is shown rotated by 90° for graphical clarity, i.e. in reality the z axis is directed straight to the left and parallel to the electron lens of the spectrometer

a further experimental difficulty to overcome. In order to measure the spin-polarization from such bands quantitatively, it has to be established that the probing spot is entirely within a single magnetic domain of known magnetization direction. In order to preserve the angular distribution of the relatively slow photoelectrons, such measurements are usually done with the sample in remanence, and preferably with in-plane magnetization if the magnetic surface so permits, in order to avoid stray fields. Best results are obtained with single crystal samples cut out in the so-called picture frame geometry [45]. A coil wound around the bottom of the frame is used to change the direction of the sample magnetization at the top, i.e. at the surface under study. Upon passing a current through the coil, essentially all magnetic flux is contained within the crystal, and the magnetization can be easily switched back and forth in the measurement position. Alternatively, the sample can be brought

into an external field coil that is preferably removed from the photoemission stage.

Control of the sample magnetization brings the further advantage that purely instrumental asymmetries in the Mott scattering, caused by slightly different detector geometries or sensitivities, or by target non-uniformities, can be cancelled by forming cross asymmetries with reversed sample magnetizations [5] (see following section).

5 Case Studies

5.1 Spin Polarization of Nickel Bulk Bands Measured on Clean Ni(111)

The Fermi surface scan in Fig. 2 showed an excellent agreement between measured contours and those obtained from a spin-polarized band structure calculation. In the latter, the spin character of the various bands is known in terms of majority and minority spin, irrespective of the actual magnetization direction. From the comparison it is straightforward to identify the respective spin states of the measured contours. Nevertheless, it is good to verify the assignment by direct measurement of the spin polarization. This is demonstrated in Fig. 6 showing spin-polarized ARPES data measured along a circular arc centered at the $[\overline{1}\overline{1}2]$ direction and following the upper rim of the plot in Fig. 2a. The top curve gives the measured intensity, showing four rather narrowly spaced peaks near the center and two larger peaks at azimuthal angles of $\sim \pm 30°$, corresponding to the "goggle"-like pattern in Fig. 2a. In the bottom curve, the experimental asymmetries are given for the same scan, measured with the two detectors of one Mott polarimeter that probe the P_z component. For this nearly grazing emission geometry ($\theta_m = 78°$), the largely in-plane magnetization vector has a strong component along the z-axis of the Mott polarimeter system when the sample azimuth is chosen appropriately [7]. The curve represents, in fact, the cross asymmetry measured along the z-axis, evaluated with two consecutive measurements with switched magnetization direction (indicated by $\oplus$ and $\ominus$):

$$A^{\otimes} = \frac{(I_L^{\oplus} + I_R^{\ominus}) - (I_R^{\oplus} + I_L^{\ominus})}{(I_L^{\oplus} + I_R^{\ominus}) + (I_R^{\oplus} + I_L^{\ominus})} \; . \tag{16}$$

This procedure removes any purely instrumental asymmetry [5] and thus establishes a dependable zero line in the asymmetry measurement[7]. One notes

---

[7] As a matter of fact, the cross asymmetry with arithmetical mean values as described in (16) is used in situations where one of the channels I_L or I_R is suspected to have a constant offset in count rate. More often the two detector channels have slightly different detection sensitivities, in which case the cross asymmetry based
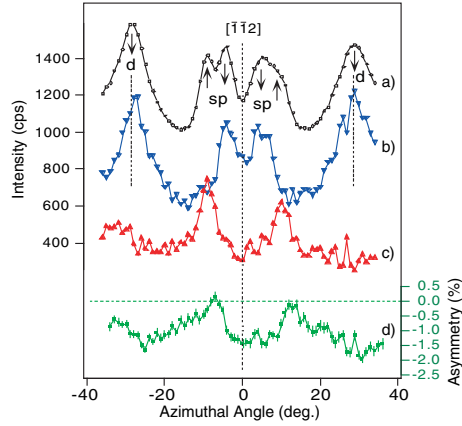
Fig. 6. (**a**) He Iα excited and spin-integrated intensity scan measured at the Fermi energy on Ni(111) along a path near the upper edge of Fig. 2a, producing an azimuthal momentum distribution curve. The peaks are annotated by their known orbital and spin assignment. Curves (**b**) and (**c**) present the spin-resolved minority and majority spin spectra, respectively, as obtained from curves (a) and (**d**) by applying (2). Curve (d) is the spin asymmetry for the polarization component measured along the sample magnetization direction (from [7]). See text for a discussion of quantitative aspects

immediately that the asymmetry values are negative (corresponding to minority spin character) throughout most of the scan, with the exception of two narrow regions where the majority *sp* band peaks are seen in the intensity curve. In between each of the two *sp* spin pairs the rapid sign change of the asymmetry manifests the different spin character of the two peaks. The assignment based on the band structure calculation (Fig. 2b) is thus correct.

From the curves a) and d) in Fig. 6 one can, in principle, calculate the spin-resolved momentum distribution curves for majority and minority spins. Before Equation 2 can be applied, one needs to translate asymmetry values into spin-polarization values. The Sherman function of the device has not been precisely measured for lack of an electron beam of known polarization. From comparison to Mott polarimeters of the same design it is known to be in the range of S = 15–25%. With these numbers the asymmetry contrast of $\Delta A_z \approx 1.2\%$ seen in Fig. 6 translates into polarization values of the order of 6% which is very low, much lower than expected from these clean exchange-split bands. This strong reduction in measured spin asymmetries

---

on geometrical mean values leads to cancellation of the unknown sensitivity factor:

$$\tilde{A}^{\otimes} = \frac{\sqrt{I_L^{\oplus} I_R^{\ominus}} - \sqrt{I_R^{\oplus} I_L^{\ominus}}}{\sqrt{I_L^{\oplus} I_R^{\ominus}} + \sqrt{I_R^{\oplus} I_L^{\ominus}}} \ . \tag{17}$$

comes from two effects: (i) The sample is only poorly magnetized; in fact the following analysis suggests a degree of magnetization of only about 12%. (ii) The direct transitions from the exchange split bands ride on an unpolarized background (signal-to-background ratio ∼0.6) that arises due to quasielastic scattering processes involving phonons, magnons and other electrons. In this particular experiment, which was carried out with a non-monochromatized He discharge lamp, a part of the background results also from photoexcitation with different photon energies $h\nu$ [7].

The second effect can be further assessed by a simple spectral synthesis model as is illustrated in Fig. 7. Fully spin-polarized Lorentzian lines are superposed on a uniform unpolarized background in order to model the intensity scan of Fig. 6a. In the model, the spin-resolved curves can be readily generated. The resulting polarization values show an amplitude of almost 50%, while we measure a much lower value of 6% indicative of a poor magnetization state of the sample. It is interesting to note that this analysis provides a nice confirmation that the uniform background underneath the direct transitions is indeed unpolarized. Any significant background polarization makes the asymmetry curve move with respect to the zero line and deform significantly from the plotted curve that agrees well with the experimental data except for the absolute scale.
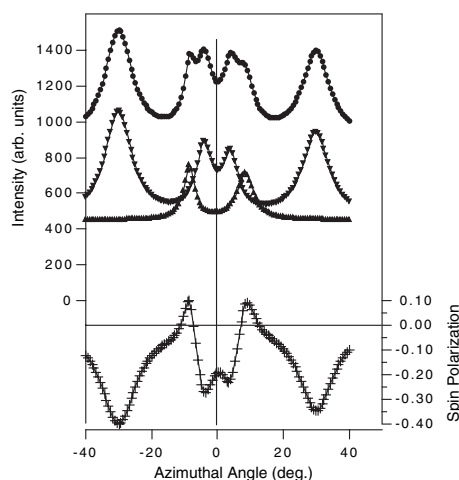

Fig. 7. (**a**) Synthesis of azimuthal intensity scan, modelling the data of Fig. 6a by using 6 Lorentzian lines of suitable positions, widths and intensities plus a constant background. The spin polarization of the individual Lorentzian lines is assumed to be +100% or −100%, respectively, depending on the majority or minority spin assignment as given in Fig. 6. The background intensity is assumed to be unpolarized. With these assumptions, the curves (**b**) and (**c**) are generated, reproducing the intensity curves for minority and majority spin electrons, respectively. The resulting spin polarization curve as calculated by (1) is shown as curve (**d**)

After the experimental asymmetry curve has been scaled up by roughly a factor of 8 to represent a fully magnetized sample, (2) can be applied to the experimental data in order to generate the spin-resolved spectra (curves b) and c) in Fig. 6). The result is quite gratifying in that it cleanly separates majority and minority bands. Note, however, that this procedure is unsuitable to study temperature-dependent spin-state mixing, which would reflect itself in reduced asymmetries for higher temperatures as the sample magnetization drops.

5.2 Spin-Polarized Surface States on Au(111)

Electronic band states can be spin-split by the spin-orbit interaction if the Kramers degeneracy, expressed as $E^{\uparrow}(\boldsymbol{k}) = E^{\downarrow}(\boldsymbol{k})$, is lifted by removing either time-reversal symmetry or inversion symmetry. Time-reversal symmetry alone demands only that $E^{\uparrow}(\boldsymbol{k}) = E^{\downarrow}(-\boldsymbol{k})$. For any crystal, inversion symmetry is naturally broken at the surface, and splittings can be expected. A remarkable example for this effect is the Shockley surface state on the Au(111) surface, representing a quasi-two-dimensional nearly-free electron gas. LaShell et al. [46] observed for this state an energy splitting that is proportional to the wave vector. Based on the Rashba term in the Hamiltonian, describing the spin-orbit interaction in propagating electronic states,

$$H_{S.O.} = \frac{\mu_B}{2c^2}(\boldsymbol{v} \times \boldsymbol{E}) \cdot \boldsymbol{\sigma} \,, \qquad (18)$$

they postulated a characteristic spin structure along the two concentric circular Fermi surfaces of the split states (see Fig. 8). In this equation, μ_B is the Bohr magneton, c the speed of light, $\boldsymbol{v}$ the group velocity of the particular state, and $\boldsymbol{\sigma}$ the vectorial spin operator. The average electric field vector $\boldsymbol{E}$ seen by the surface state electrons is perpendicular to the surface and pointing outside. Due to the vector product, the spin vector is thus expected to be entirely in-plane and perpendicular to the velocity vector, i.e. tangential to the Fermi surface. In the proposed spin structure, the spin vectors of the outer state, i.e. the state that has its energy lowered by the spin-orbit interaction to produce a larger Fermi surface, follow the contour in an anti-clockwise sense, while those of the inner state do so in a clockwise sense.

Spin-polarized ARPES with three-dimensional spin polarimetry has been applied to verify the spin polarization [47] and the spin structure [48] of the spin-orbit split Au(111) surface state. Figure 9a shows angle-resolved energy distribution curves for five different angles probing the dispersion of the state. The energy resolution has been much relaxed with respect to the data shown in Fig. 8d because of the low efficiency of the spin detectors and the very high number of electron counts needed for reliable spin analysis (typically 10^5 electrons). The energy splitting in the spectra is no longer observed in the raw intensity spectra, it is just reflected in an increased line width of the peak at polar angles of $\pm 3.5°$. At $\pm 4.5°$ the inner state
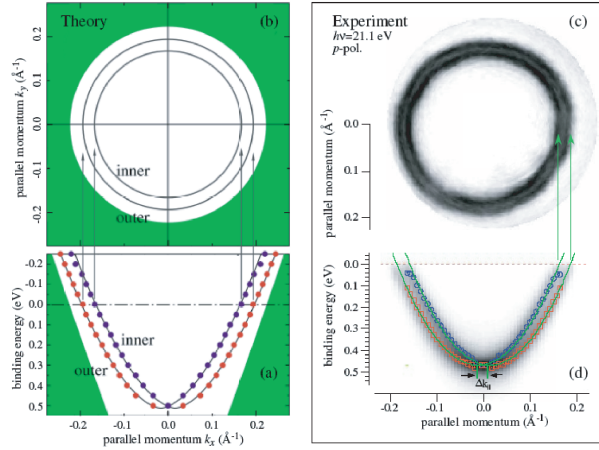
Fig. 8. Spin-orbit splitting of the Au(111) Shockley surface state found in the energy gap near the L-point of the bulk Brillouin zone. (**a**) The dispersion along k_x of the inner and outer surface state, as obtained from a first-principles calculation. The region of bulk bands is shaded in gray. (**b**) The theoretical momentum distribution of the surface states at the Fermi energy. (**c**) The experimental Fermi surface map, as obtained from a spin-integrated high-resolution photoemission experiment. (**d**) The experimental dispersion map in an arbitrary azimuth. The peak positions as determined from peak fitting to the energy distribution curves are indicated by circles, and parabolic fits to these positions are shown by solid lines. In both experimental panels, the measured intensities are shown in a linear gray scale, with black corresponding to the highest intensity (from [49])

has already crossed the Fermi level and the peak is again narrower. The polarization spectra reveal the spin polarization of the split states. The in-plane polarimeter component tangential to the Fermi surface is shown, as well as the out-of-plane component. Whereas there is no significant in-plane polarization at normal emission, where the state is not split, a characteristic polarization pattern develops in both directions with increasing polar angle. Depending on the sign of the polar angle θ_m, the polarization values are first negative or positive and switch sign roughly at the peak position. Maximum observed in-plane polarization values are of the order of 50%. On the other hand, there is no out-of-plane polarization visible in this data.

Unlike in the case of magnetized Ni(111) in the previous section, the polarization values do not depend on the sample magnetization. Except for a contribution from some unpolarized background, one should expect each state to be nearly 100% polarized. Reduced values arise from the spectral overlap of the two split components. Polarization modelling has been done along the lines discussed in the context of Fig. 7. For the observed line width, resulting from both the energy resolution of 120 eV and from the angular resolution of 1.2° that samples more states as the dispersion gets steeper, a
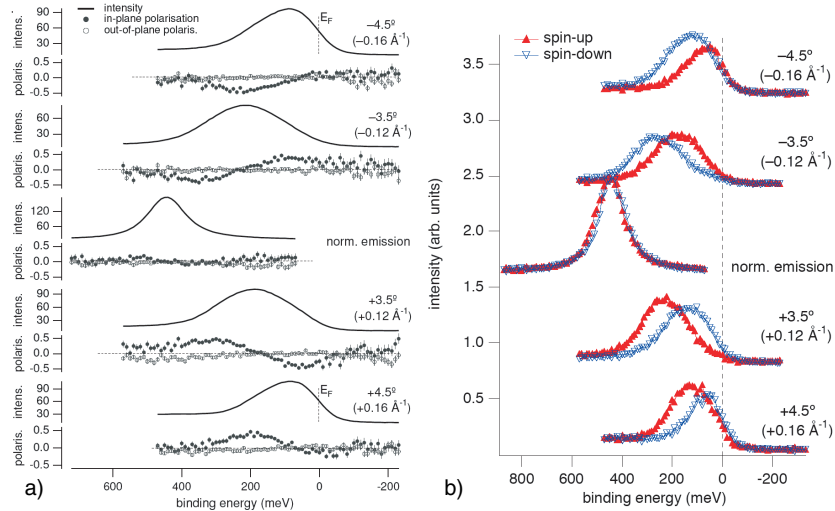
Fig. 9. Spin-polarized photoemission measurements of the Shockley surface state on Au(111) at several emission angles. (**a**) The top curves of each data set show the intensity measured by four channels of one of the Mott polarimeters. The lower curves give the measured polarization values determined from the in-plane and out-of-plane components of the polarization vector, using the relation $P = (1/S_{eff})(I_L - \eta I_R)/(I_L + \eta I_R)$ for the appropriate detector channels, with effective Sherman functions S_{eff} of 0.1–0.15 and relative gain factors $\eta \approx 0.97 - 1.03$ for the two scattering planes. The latter are used in order to compensate for the instrumental asymmetry. The spectrometer resolution was set to 120 meV and $1.2°$ full width at half maximum, respectively. (**b**) Spin-resolved spectra as derived from the data in a) by using (2) and the in-plane polarization values (from [47])

measured polarization value of 50% is consistent with spin-split states that are essentially ±100% polarized without any significant unpolarized background.

The data of Fig. 9 are also consistent with the spin structure proposed by LaShell et al.: The measurement of the polarimeter channels for P_x and P_y show that the strong in-plane polarization signal is in the direction tangential to the Fermi surface, defined by $P_{tan} = (P_x + P_y)/\sqrt{2}$ [47]. Moreover, when probing the spin polarization of, e.g. the outer state on opposite sides of the Fermi surface, i.e. at $\pm\theta_m$, the in-plane polarization switches sign, so that we have indeed $E^\uparrow(\boldsymbol{k}) = E^\downarrow(-\boldsymbol{k})$. In a similar fashion, the spin structure on a hydrogen-saturated W(110) surface has been shown to circulate in a counterclockwise sense around a hole pocket in the Fermi surface, corresponding here to the "inner state" [50]. The opposite sense of rotation of the inner state is related to the hole-like character of these states.

For further confirmation of this spin structure, the apparatus described in Sect. 4 can produce a complete spin-resolved momentum distribution map of the surface state [48]. This is demonstrated in Fig. 10 which is the first data
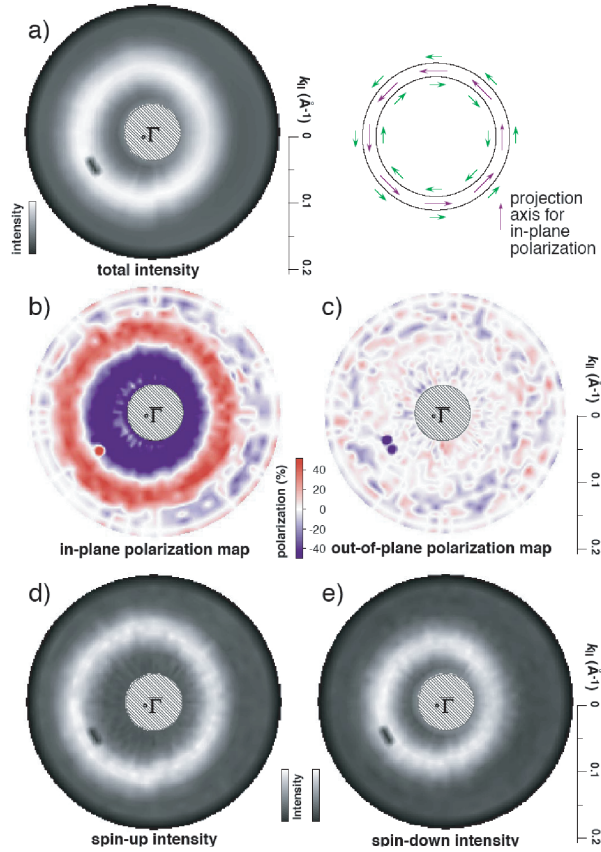
Fig. 10. Measured spin-resolved momentum distribution maps for a binding energy of 170 meV using ultraviolet light of 21.1 eV photon energy. The top panel (**a**) shows the total intensity map and a sketch of the predicted spin structure. Purple arrows indicate the rotating projection axis for in-plane polarization. The center panels (**b**) and (**c**) show the polarization maps for the in-plane and out-of-plane component of the polarization vector. The in-plane polarization (b) is a projection on the tangents to the circular Fermi surface. Red (blue) indicates a counterclockwise (clockwise) spin orientation. The bottom panels show the individual spin-up (**d**) and spin-down (**e**) intensity maps derived from a) and b) by applying (2). Note the different radii of the two Fermi surfaces of the individual bands. These data consisting of 1080 angular settings were measured in 6 h. The shift of the common center of the circles with respect to the center of the graphs is due to a 0.5° misalignment of the sample rotation axis (from [48])

set of its kind. In order to increase the count rate by a factor of two, these data have been measured at a binding energy of 170 meV, where the Fermi-Dirac distribution function is already saturated. Due to the relaxed energy and angular resolution, the spin-split states are not resolved in the intensity

panel a), like in Fig. 9a. Nevertheless, the states can be separated by the measurement of the strong in-plane polarization signal (Fig. 10b). It should be noted that, since motion along the circular state is achieved by rotating the sample about the surface normal (angle ϕ_m), the in-plane polarization is always measured directly as P_{tan}, which is thus the natural coordinate frame for this measurement. This is no longer true for states that are non-symmetric with respect to rotations about ϕ_m. By applying (2) to all individual data points, the spin-resolved momentum maps can be produced (panels d) and e)). They show circular momentum distributions with clearly different radii that correspond well to the values that can be extracted for inner and outer states from the high-resolution dispersion data of Fig. 8d. On the other hand, the out-of-plane polarization map shows values scattered around 0% without any significant structure. From a detailed analysis of these data, systematic modulations of this polarization component that would be consistent with the symmetry of the surface can be excluded at a level of 5% polarization amplitude [49].

6 Outlook

Up to this date, spin-polarized photoemission experiments have been carried out by a small number of dedicated groups. This is mainly due to the low efficiency of current spin detectors, making such experiments difficult and time consuming. Applications have been mainly in the field of surface and interface magnetism and ultrathin magnetic films. The author believes that the situation is currently changing. ARPES has been a major player in the study of strongly correlated electron systems and has brought significant advances e.g. in the understanding of high-temperature superconductivity or colossal magnetoresistance. With very few exceptions [51, 52], none of the hundreds of experimental studies have directly exploited the electron spin, which is a key feature in electron correlation physics. As soon as spin-resolved photoemission spectrometers become more readily available, there will be a strong scientific case to use them. Indeed, manufacturers of high-resolution spectrometers now offer complete solutions for adding spin detection to their systems. If, one day in the future, the spin-detectors based on electron scattering asymmetries could be replaced by much more efficient devices based e.g. on spin-dependent electron absorption [53], the technique would experience a tremendous boost.

and Jürgen Henk. He is grateful to Hans-Christoph Siegmann for critically reading the manuscript, and for contributing a large part of Sect. 3.4.

References

1. S. Hüfner: *Photoelectron Spectroscopy: Principles and Applications*, 3rd edn. (Springer, Berlin Heidelberg New York 2003)
2. S. A. Wolf, D. D. Awschalom, R. A. Buhrman, J. M. Daughton, S. von Molnar, M. L. Roukes, A. Y. Chtchelkanova, D. M. Treger, Science **294**, 1488 (2001)
3. S. Datta, B. Das: Appl. Phys. Lett. **56**, 665 (1990)
4. N. F. Mott, H. S. W. Massey: *The Theory of Atomic Collisions* (Clarendon, Oxford 1965), Chap. IX
5. J. Kessler: *Polarized Electrons*, 2nd edn. (Springer, Berlin Heidelberg 1985)
6. R. Matzdorf: Surf. Sci. Rep. **30**, 153 (1998)
7. M. Hoesch, T. Greber, V. N. Petrov, M. Muntwiler, M. Hengsberger, W. Auwärter, J. Osterwalder: J. Electron Spectrosc. Relat. Phenom. **124**, 263 (2002)
8. K. Schwarz, P. Blaha, G. K. H. Madsen: Comput. Phys. Commun. **147**, 71 (2002)
9. V. N. Strocov, R. Claessen, G. Nicolay, S. Hüfner, A. Kimura, A. Harasawa, S. Shin, A. Kakizaki, P. O. Nilsson, H. I. Starnberg, P. Blaha: Phys. Rev. Lett. **81**, 4943 (1998)
10. T. J. Kreutz, T. Greber, P. Aebi, J. Osterwalder: Phys. Rev. B **58**, 1300 (1998)
11. H. C. Siegmann: Surf. Sci. **307**, 1076 (1994)
12. M. Grioni: A Photoemission Primer. In: *Magnetism and Synchrotron Radiation*, Lecture Notes in Physics, vol 565, ed by E. Beaurepaire, F. Scheurer, G. Krill, J.-P. Kappler (Springer, Berlin Heidelberg New York 2001) pp 109–129
13. S. Monastra, F. Manghi, C. A. Rozzi, C. Arcangeli, E. Wetli, H.-J. Neff, T. Greber, J. Osterwalder: Phys. Rev. Lett. **88**, 236402 (2002)
14. U. Alkemper, C. Carbone, E. Vescovo, W. Eberhardt, O. Rader, W. Gudat: Phys. Rev. B **50**, 17496 (1994)
15. M. Getzlaff, J. Bansmann, J. Braun, G. Schönhense: J. Magn. Magn. Mat. **161**, 70 (1996)
16. D. T. Pierce, F. Meier: Phys. Rev. B **13**, 5484 (1976)
17. D. T. Pierce, R. J. Celotta, G.-C. Wang, W. N. Unertl, A. Galejs, C. E. Kuyatt, S. R. Mielczarek: Rev. Sci. Instrum. **51**, 478 (1980)
18. U. Heinzmann, G. Schönhense: Spin-Resolved Photoemission from Nonmagnetic Metals and Adsorbates. In: *Polarized Electrons in Surface Physics*, ed by R. Feder (World Scientific, Singapore 1985) pp 467–512
19. H. P. Oepen, K. Hünlich: J. Kirschner, Phys. Rev. Lett. **56**, 496 (1986)
20. E. Tamura, W. Piepke, R. Feder: Phys. Rev. Lett. **59**, 934 (1987)
21. E. Tamura, R. Feder: Europhys. Lett. **16**, 695 (1991)
22. J. Henk, R. Feder: Europhys. Lett. **28**, 609 (1994)
23. B. Schmiedeskamp, B. Vogt, U. Heinzmann: Phys. Rev. Lett. **60**, 651 (1988)
24. N. Irmer, R. David, B. Schmiedeskamp, U. Heinzmann: Phys. Rev. B **45**, 3849 (1992)
25. N. Irmer, R. Frentzen, S.-W. Yu, B. Schmiedeskamp, U. Heinzmann: J. Electron Spectrosc. Relat. Phenom. **78**, 321 (1996)

26. C. S. Fadley, D. A. Shirley, A. J. Freeman, P. S. Bagus, J. V. Mallow: Phys. Rev. Lett. **23**, 1397 (1969); C. S. Fadley, D. A. Sirley, Phys. Rev. A **2**, 1109 (1970)
27. B. Sinkovic, B. Hermsmeier: C. S. Fadley, Phys. Rev. Lett. **55**, 1227 (1985)
28. D. P. Pappas, K.-P. Kämpfer, B. P. Miller, H. Hopster, D. E. Fowler, C. R. Brundle, A. C. Luntz, Z.-X. Shen: Phys. Rev. Lett. **66**, 504 (1991)
29. H. C. Siegmann: J. Electron Spectrosc. Relat. Phenom. **68**, 505 (1994)
30. D. Oberli, R. Burgermeister, S. Riesen, W. Weber, H. C. Siegmann: Phys. Rev. Lett. **81**, 4228 (1998)
31. W. Weber, S. Riesen and H. C. Siegmann: Science **291**, 1015 (2001)
32. R. L. Long, Jr., V. W. Hughes, J. S. Greenberg, I Ames, and R. L. Christensen: Phys. Rev. A **138**, 1630 (1965)
33. A. B. Baganov, and D. B. Diatroptov: Zh Eksp. Teor. Fiz. **54**, 1333 (1968) (Sov. Phys.-JETP **27**, 1733 (1968))
34. G. Busch, M. Campagna, P. Cotti, H. C. Siegmann: Phys. Rev. Lett. **22**, 597 (1969)
35. U. Baenninger, G. Busch, M. Campagna, H. C. Siegmann: Phys. Rev. Lett. **25**, 585 (1970)
36. W. Eib and S. F. Alvarado: Phys. Rev. Lett. **37**, 444 (1976)
37. G. Busch, M. Campagna, D. T. Pierce, H. C. Siegmann: Phys. Rev. Lett **28**, 611 (1972)
38. J. C. Gröbli, A. Kündig, F. Meier, and H. C. Siegmann: Physica B **204**, 359 362 (1995)
39. M. Taborelli, R. Allenspach, G. Boffa, and M. Landolt: Phys. Rev. Lett **56**, 2869 (1986)
40. O. M. Paul: Ph. D Thesis. ETH Zürich Nr. **9210** (1990)
41. F. Meier, D. Pescia, M. Baumberger: Phys. Rev. Lett. **49**, 747 (1982)
42. F. Meier, G. L. Bona, S. Hüfner: Phys. Rev. Lett. **52**, 1152 (1984)
43. M. Aeschlimann, M. Bauer, and S. Pawlik: Phys. Rev. Lett. **79**, 5158 (1997)
44. A. Vaterlaus, F. Milani, and F. Meier: Phys. Rev. Lett. **65**, 3041 (1990)
45. M. Donath: Surf. Sci. Rep. **20**, 251 (1994)
46. S. LaShell, B. A. McDougall, E. Jensen: Phys. Rev. Lett. **77**, 3419 (1996)
47. M. Muntwiler, M. Hoesch, V. N. Petrov, M. Hengsberger, L. Patthey, M. Shi, M. Falub, T. Greber, J. Osterwalder: J. Electron Spectrosc. Relat. Phenom. **137–140**, 119 (2004)
48. M. Hoesch, M. Muntwiler, V. N. Petrov, M. Hengsberger, L. Patthey, M. Shi, M. Falub, T. Greber, J. Osterwalder: Phys. Rev. B **69**, 241401(R) (2004)
49. J. Henk, M. Hoesch, J. Osterwalder, A. Ernst, P. Bruno: J. Phys. Condens. Matter **16**, 7581 (2004)
50. M. Hochstrasser, J. G. Tobin, E. Rotenberg, S. D. Kevan: Phys. Rev. Lett. **89**, 216802 (2002)
51. N. B. Brookes, G. Ghiringhelli, O. Tjernberg, L. H. Tjeng, T. Mizokawa, T. W. Li, A. A. Menovsky: Phys. Rev. Lett. **87**, 237003 (2001)
52. J. H. Park, E. Vescovo, H. J. Kim, C. Kwon, R. Ramesh, T. Venkatesan: Phys. Rev. Lett. **81**, 1953 (1998)
53. M. Erbudak, G. Ravano: J. Appl. Phys. **52**, 5032 (1981)